

# Plasma waves confined to the diamagnetic cavity of comet 67P/Churyumov–Gerasimenko

H. Gunell,<sup>1,2\*</sup> C. Goetz,<sup>3</sup> A. Eriksson,<sup>4</sup> H. Nilsson,<sup>5</sup> C. Simon Wedlund,<sup>6</sup> P. Henri,<sup>7</sup>  
R. Maggiolo,<sup>1</sup> M. Hamrin,<sup>2</sup> J. De Keyser,<sup>1</sup> M. Rubin,<sup>8</sup> G. Stenberg Wieser,<sup>5</sup>  
G. Cessateur,<sup>1</sup> F. Dhooghe<sup>1</sup> and A. Gibbons<sup>1,9</sup>

<sup>1</sup>Royal Belgian Institute for Space Aeronomy (BIRA-IASB), Avenue Circulaire 3, B-1180 Brussels, Belgium

<sup>2</sup>Department of Physics, Umeå University, SE-901 87 Umeå, Sweden

<sup>3</sup>Institut für Geophysik und extraterrestrische Physik, TU Braunschweig, Mendelssohnstr. 3, D-38106 Braunschweig, Germany

<sup>4</sup>Swedish Institute of Space Physics, Ångström Laboratory, Lägerhyddsvägen 1, SE-75121 Uppsala, Sweden

<sup>5</sup>Swedish Institute of Space Physics, Box 812, SE-981 28 Kiruna, Sweden

<sup>6</sup>Department of Physics, University of Oslo, Box 1048 Blindern, 0316 Oslo, Norway

<sup>7</sup>LPC2E, CNRS, F-45071 Orléans, France

<sup>8</sup>Physikalisches Institut, University of Bern, Sidlerstrasse 5, CH-3012 Bern, Switzerland

<sup>9</sup>Laboratoire de Chimie Quantique et Photophysique, Université Libre de Bruxelles, 50 Avenue F. D. Roosevelt, B-1050 Brussels, Belgium

Accepted 2017 May 5. Received 2017 May 4; in original form 2017 March 30

## ABSTRACT

Ion acoustic waves were observed in the diamagnetic cavity of comet 67P/Churyumov–Gerasimenko by the *Rosetta* spacecraft on 2015 August 3, when the comet was 1.25 au from the Sun. Wave spectra recorded by the Langmuir probe (RPC-LAP), peak near 200 Hz, decrease for higher frequencies and reach the noise floor at approximately 1.5 kHz. These waves were observed only when the spacecraft was in the diamagnetic cavity or at its boundary, which is identified as a sharp drop in magnetic field magnitude, measured by RPC-MAG. The plasma, on both sides of the boundary, is dominated by a cold (a few hundred K) water group ion population, one cold ( $k_B T_e \sim 0.1$  eV) and one warm ( $k_B T_e \sim 10$  eV) electron population. The observations are interpreted in terms of current-driven ion acoustic waves, generated by currents that flow through bulges on the boundary of the diamagnetic cavity.

**Key words:** plasmas – waves – methods: analytic – methods: data analysis – comets: individual: 67P/Churyumov-Gerasimenko.

## 1 INTRODUCTION

The first observation of the diamagnetic cavity at a comet was made when the *Giotto* spacecraft flew by Comet Halley in 1986 (Neubauer et al. 1986). During two minutes around *Giotto*'s closest approach to the comet's nucleus, the spacecraft passed through a region where the magnetic field was approximately zero. The phenomenon had already been observed at the AMPTE (Active Magnetospheric Particle Tracer Explorer) artificial comet, created by the release of barium in the solar wind (Haerendel et al. 1986). It was shown using analytic models that a diamagnetic cavity can be maintained by a balance between the magnetic pressure of the solar wind and the ion–neutral friction force, stemming from the expanding neutral atmosphere of the comet (Cravens 1987; Haerendel 1987).

The *Rosetta* spacecraft (Glassmeier et al. 2007a) followed comet 67P/Churyumov–Gerasimenko from 2014 August, through its

approach of the Sun, reaching perihelion at 1.24 au in 2015 August, and continuing its journey outward again until the mission ended in 2016 September. Encounters of the diamagnetic cavity were identified in magnetic field data between 2015 April and 2016 February (Goetz et al. 2016a), the first encounter published from this mission was detected on 2015 July 26 and lasted 25 min (Goetz et al. 2016b). The nucleus to spacecraft distance was generally larger than the cavity radius that had been predicted by simulations (e.g. Koenders et al. 2015; Rubin et al. 2015). Observations by Goetz et al. (2016a) and Henri et al. (2017) indicate that the shape of the cavity is not stationary. Instead bulges form on the boundary due to an instability, and the short duration of the periods the spacecraft spent in the cavity corresponds to the duration of such a bulge passing over the spacecraft. The spacecraft velocity in the comet frame of reference is typically less than  $1 \text{ m s}^{-1}$ . A dropout of suprathermal electrons at energies of 200 eV as the spacecraft entered the cavity was found by Nemeth et al. (2016).

The plasma environment of comet 67P/Churyumov–Gerasimenko was surveyed by Odelstad et al. (2015) for the

\* E-mail: herbert.gunell@physics.org

period up to and including 2015 March. They reported electron temperatures,  $T_e$ , around 5 eV. Eriksson et al. (2017) found that a much colder ( $k_B T_e \lesssim 0.1$  eV) electron population became more abundant later in the mission. The electron population is cooled by collisions with the neutrals, if the neutral density is high enough (Vigren & Galand 2013). Most of the time, the *Rosetta* spacecraft was located outside the region where this cooling process is efficient (Mandt et al. 2016). Ion measurements in the low-mass loading regime showed ions following the first part of a cycloid trajectory (Nilsson et al. 2015a), as has been illustrated by simulations (Gunell et al. 2015; Simon Wedlund et al. 2017). Later, at higher mass loading, water group ion trajectories turned more antisunward (Nilsson et al. 2015b; Behar et al. 2016a). Simon Wedlund et al. (2016) used measurements of the  $\text{He}^+$  to  $\text{He}^{2+}$  ratio to estimate the neutral outgassing rate. Hybrid simulations have been used to evaluate the ion measurements at different heliocentric distances during the mission (Behar et al. 2016b; Simon Wedlund et al. 2017). The ion environment throughout *Rosetta*'s accompaniment of comet 67P/Churyumov–Gerasimenko was described by Nilsson et al. (2017). Low-frequency waves were found in the magnetic field spectrum shortly after *Rosetta* arrived at the comet (Richter et al. 2015, 2016). Karlsson et al. (2017) detected signals of lower hybrid waves in the electric field spectrum at 1.5 au heliocentric distance. Solar wind interaction with comets in light of the *Rosetta* mission was further reviewed by Glassmeier (2017).

An ion acoustic wave is a compressional plasma wave at frequencies below the ion plasma frequency. In the long wavelength limit, the frequency of an ion acoustic wave is proportional to its wavenumber. Ion acoustic waves are heavily damped unless  $T_e \gg T_i$ , the ion temperature. However, even in the heavily damped regime, they may still be driven unstable by the presence of a current (Stringer 1964). The *ICE* spacecraft detected ion acoustic waves in the bow shock region of comet Giacobini–Zinner (Scarf et al. 1986), and such waves were also found in the foreshock upstream of Comet Halley (Oya et al. 1986). Waves were observed in the diamagnetic cavity of the AMPTE artificial comet, and ion acoustic waves were deemed a possible explanation for the low-frequency emission bands observed (Gurnett et al. 1985).

At comet 67P/Churyumov–Gerasimenko, Gunell et al. (2017) studied one day of data, obtained by *Rosetta* on 2015 January 20, and found evidence for ion acoustic waves. The comet was then at a heliocentric distance of 2.5 au; the comet–solar wind interaction was dominated by weak mass loading, and no diamagnetic cavity had formed. In this paper, we report observations of ion acoustic waves in the diamagnetic cavity of comet 67P/Churyumov–Gerasimenko in early 2015 August, close to perihelion, at a heliocentric distance of 1.25 au. From the perspective of ion acoustic waves, the most significant difference in plasma properties between the two dates is the presence of a significant cold electron population in the near-perihelion observations reported here.

## 2 OBSERVATIONS

We use the Langmuir Probe instrument (RPC-LAP; Eriksson et al. 2007) to observe ion acoustic waves in the diamagnetic cavity, which is identified in magnetic field measurements by the RPC-MAG instrument (Glassmeier et al. 2007b). The interpretation of the wave observations is aided by measurements of ion distributions by the Ion Composition Analyzer of the Rosetta Plasma Consortium (RPC-ICA; Nilsson et al. 2007), current–voltage characteristics obtained

by RPC-LAP, and plasma density measurements by the Mutual Impedance Probe (RPC-MIP; Trotignon et al. 2007).

### 2.1 Cavities

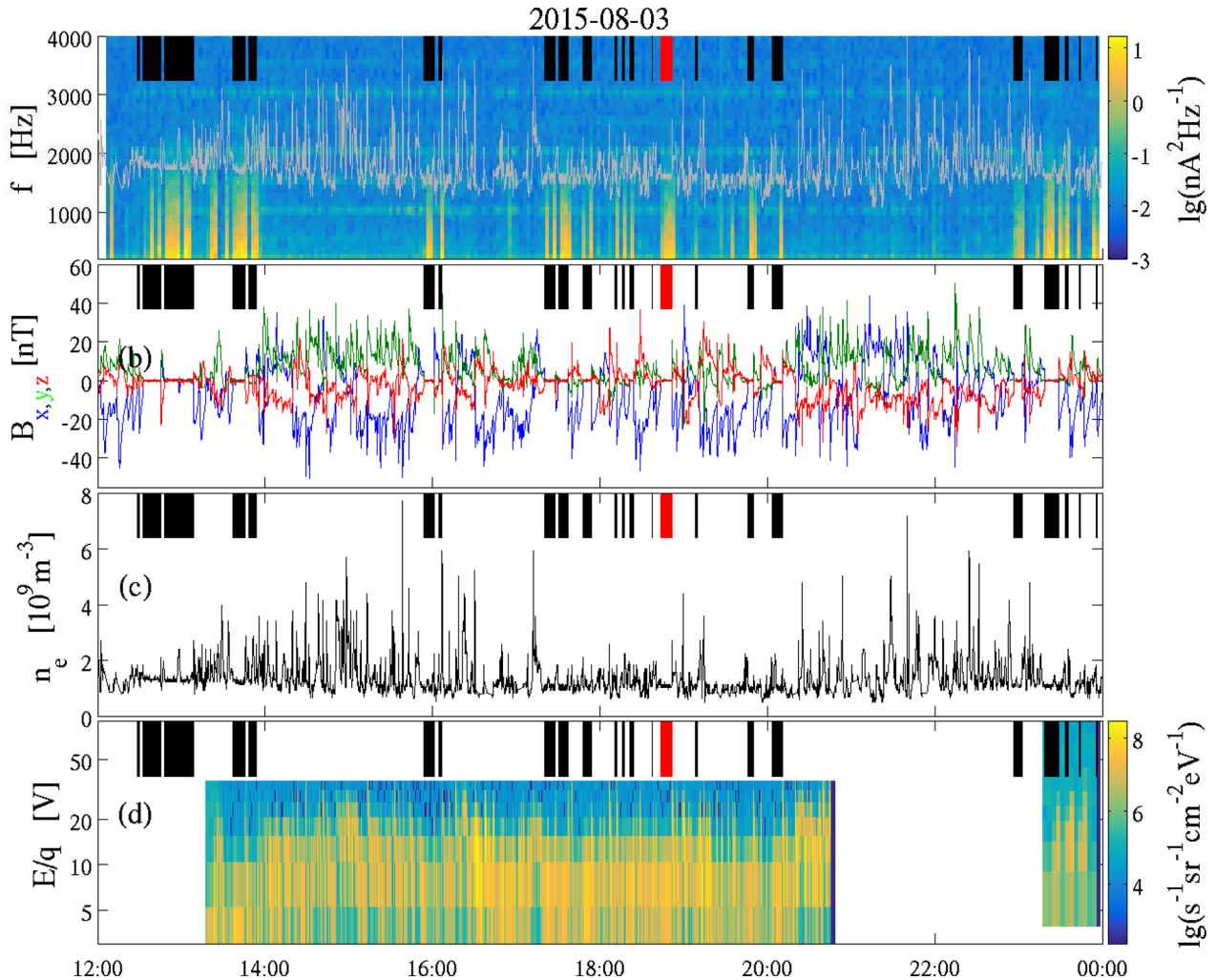
The diamagnetic cavity is identified in the magnetometer data as a sharp decrease of the magnetic field, as the spacecraft enters the cavity, followed by a period of low and unchanging magnetic field, which lasts until the spacecraft exits the cavity (Goetz et al. 2016a). The magnetometer has a temperature-dependent offset, which complicates the analysis. However, by assuming that the average magnetic field is zero inside the cavity, a temperature model of the magnetometer has been constructed and used to correct the rest of the data, which consistently shows near-zero values of the magnetic field in the cavity. While the in-cavity field is not necessarily zero, its magnitude can be confined to  $B < 1$  nT for the parts of the diamagnetic cavity that have been visited by *Rosetta*. Goetz et al. (2016a) identified 665 intervals when *Rosetta* passed through the diamagnetic cavity. In the following sections, we use their list of cavity identifications as well as their instrument-temperature-corrected magnetic field data set. From this list, we have picked one day, 2015 August 3, to study in more detail. We first present an overview of that day, and then details from one sample cavity encounter that occurred during the day.

Fig. 1 shows the power spectral density,  $P_{II}$ , of the current to the RPC-LAP probe 1, the three components of the  $\mathbf{B}$  field, the plasma density measured by RPC-MIP and the differential particle flux of the ions summed over all RPC-ICA viewing directions during 12 h on 2015 August 3, when the comet was at 1.25 au heliocentric distance and the spacecraft at 220 km cometocentric distance. The periods when the spacecraft passed through the diamagnetic cavity, as identified by Goetz et al. (2016a), are marked by black rectangles in all three panels. The cavity that is marked by a red rectangle is shown in detail in Fig. 2.

### 2.2 Waves

The power spectral densities shown in Figs 1 and 2 have been computed from time series data obtained by RPC-LAP, which records the current to the two probes at a sampling frequency of 18 750 Hz in the mode used here. Each time series comprises 1600 samples, and is thus 85.3 ms long. These time series are recorded at 160 s intervals. The white spaces between the colour-coded spectra in Fig. 2(a) correspond to the times when no time series were recorded. In Fig. 1, the spectra have been allowed to cover the white spaces to enable viewing of the whole 12-h period. During the recording of the time series, probe 1 was biased to +30 V and probe 2 to –30 V with respect to the spacecraft potential. No discernible wave signal could be found on the negatively biased probe 2, and therefore only spectra obtained by probe 1 are shown in the figures. The absence of a wave signal on the negatively biased probe shows that the measured current is dominated by electrons, and the observed signal is therefore proportional to the plasma density variations of the wave.

The spectra in Fig. 2(a) are also shown as line plots in Fig. 3. The power spectral density recorded when the spacecraft was in the cavity (solid lines) was much higher than that recorded outside the cavity (dashed lines). The solid black line shows the spectrum recorded at 18:43:12 when the spacecraft was at the boundary of the diamagnetic cavity, and it falls between the two groups in Fig. 3. The plasma density, although highly variable in the magnetized regions, was fairly stable from one cavity encounter to the next. In the cavity it was  $n_e \approx 1.0 \times 10^9 \text{ m}^{-3}$ , as seen in Fig. 2(c). Assuming that all



**Figure 1.** Overview of the observations by the RPC instruments on board the *Rosetta* spacecraft during the second half of 2015 August 3. (a) Power spectral density of the current to Langmuir probe 1 in the frequency range of  $200 \text{ Hz} < f \leq 4 \text{ kHz}$ . The grey curve shows the  $\text{H}_2\text{O}^+$  ion plasma frequency. (b) Components of the magnetic flux density  $\mathbf{B}$  seen by RPC-MAG. (c) Plasma density measured by the RPC-MIP instrument. (d) Ion energy spectrum measured by RPC-ICA. The colour-coded quantity is the differential particle flux summed over all viewing directions. The energy scale has been adjusted for  $V_{\text{sc}}$  and  $V_{\text{offset}}$ . The black rectangles shown at the top of each panels mark periods when the spacecraft was inside the diamagnetic cavity, as identified by Goetz et al. (2016a). The red rectangles mark the cavity passage that is shown in more detail in Fig. 2.

ions are  $\text{H}_2\text{O}^+$  ions, this means that the ion plasma frequency was  $f_{\text{pi}} \approx 1.6 \text{ kHz}$ .

The wave spectra observed inside the diamagnetic cavity show a broad peak near 200 Hz and fall off slowly at higher frequencies, reaching the noise floor near the ion plasma frequency. In Fig. 3, the peaks that are seen at 1.0, 1.5 and 2.0 kHz are artefacts generated by the spacecraft. These are also seen as horizontal stripes in Fig. 1(a). The lowest frequency bins are liable to pick up low-frequency noise, and therefore the colour-coded spectra in Figs 1(a) and 2(a) are shown only for frequencies above 200 Hz.

Fig. 2 shows that the waves appear only in the diamagnetic cavity or at the boundary. In Fig. 1, waves are seen during the spacecraft’s traversals of the cavity. During the 12-h span of the figure, there are a few cases, for example, at 12:08 and 13:20, of wave signals registered during periods that were not identified as cavity passages. To examine these cases in more detail, we investigate the relationship between wave activity and the spacecraft position relative to the boundary of the diamagnetic cavity. We integrate the power spec-

tral density in the range of  $200 \text{ Hz} < f < 1500 \text{ Hz}$  obtaining the power

$$\int_{200 \text{ Hz}}^{1500 \text{ Hz}} P_{\text{II}}(f) df$$

for each time series. The integral is normalized to the highest value during the day, and this is shown in Fig. 4 together with the magnitude of the magnetic flux density  $B$  normalized in the same way. In the figure, the cavities are marked by light blue areas.

There are two reasons why high wave power values are observed outside these regions. First, the waves exist not only inside the cavity proper, but also at the boundary. In the example of the peak in wave power at 12:08 (the first panel of Fig. 4), a decrease in  $B$  was observed just before the wave spectrum was recorded, indicating that the spacecraft was in the boundary region but did not pass completely through it into the cavity itself. Another example is the black curve in Fig. 3, which was recorded at the boundary and shows a power spectral density between those obtained completely

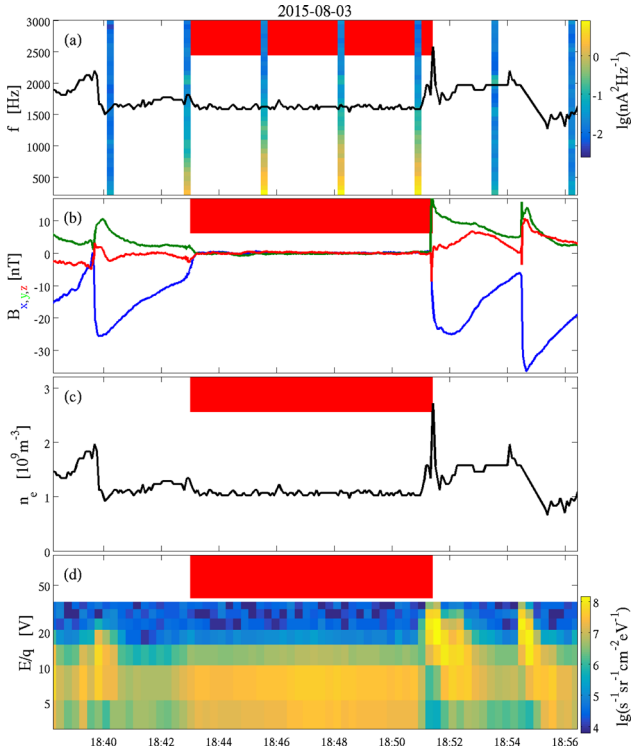


**Figure 2.** Details of the data from a single passage through the diamagnetic cavity. (a) Power spectral density of the current to Langmuir probe 1 in the frequency range of  $200 \text{ Hz} < f \leq 3 \text{ kHz}$ . The black curve shows the  $\text{H}_2\text{O}^+$  ion plasma frequency. (b) The three components of the magnetic flux density  $B$  seen by RPC-MAG. (c) Plasma density measured by the RPC-MIP instrument. (d) Ion energy spectrum measured by RPC-ICA. The colour-coded quantity is the differential particle flux summed over all viewing directions. The energy scale has been adjusted for  $V_{\text{sc}}$  and  $V_{\text{offset}}$ . The red rectangles mark the duration of the cavity, as it was identified by Goetz et al. (2016a).

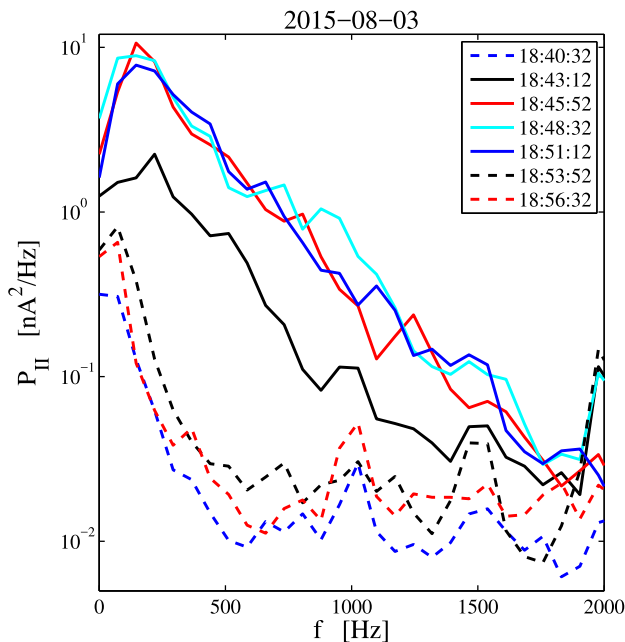


**Figure 3.** Line plots of the spectra for the cavity encounter shown in Fig. 2(a). The dashed lines show spectra obtained outside the cavity. The black solid line shows the spectrum recorded at 18:43:12 when the spacecraft was at the boundary, about to enter the cavity.

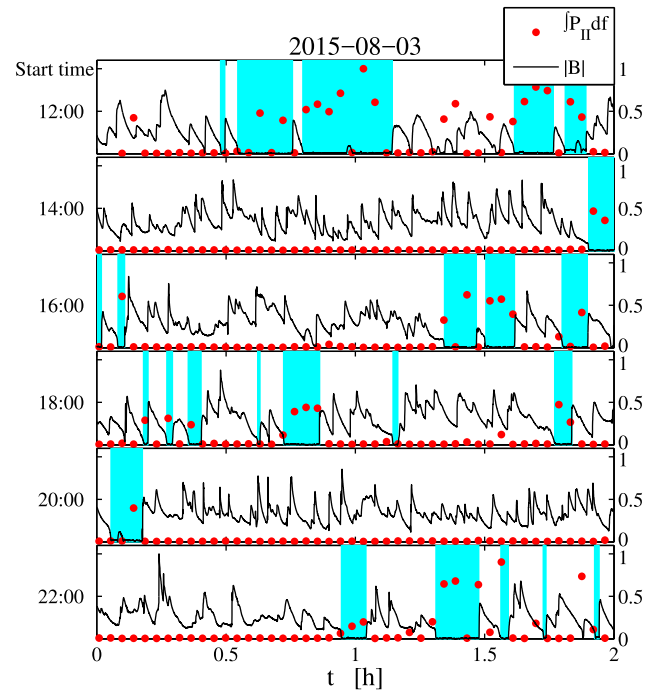


**Figure 4.** The power spectral density integrated over the interval  $200 \text{ Hz} < f < 1500 \text{ Hz}$  (red dots) and the magnitude of the magnetic flux density  $B$  (black line). Both quantities have been normalized to the highest value observed during the 12-h period. Each panel shows two hours of observations. The light blue areas mark the cavities identified by Goetz et al. (2016a).

inside and completely outside the boundary. Secondly, short cavity traversals may comprise too few magnetic field data points to allow identification. Since the time between wave observations is 160 s it may also happen that a complete cavity sighting happens when no wave measurement is performed.

To conclude this section, we note that during this day, the waves were observed in the diamagnetic cavity and at its boundary, but not elsewhere.

### 2.3 Ion populations

The RPC-ICA instrument (Nilsson et al. 2007) measures the differential particle flux of ions in 16 sectors. During the period shown in Fig. 2, and most of that shown in Fig. 1, the instrument was operated in a high temporal resolution mode, where no scanning out of the nominal viewing plane was performed, and the energy sweep was reduced to eight energy channels covering a range from 15 to 56 eV. One such energy sweep was performed every 16 s. Ion distribution functions are derived from the RPC-ICA data in the way described by Gunell et al. (2017). An offset to the energy scale was found when measurements first were performed at the comet (Nilsson et al. 2015a). In this work, we use an energy table that has been corrected accordingly (Nilsson et al. 2017; Stenberg Wieser et al. 2017). The spacecraft potential is determined by finding the value which puts the lowest energy ions at zero velocity. For 2015 August 3, the spacecraft potential value found in this way is  $-16.3 \text{ V}$ . However, in the high temporal resolution mode, the energy sweep does not cover the lowest energies. This means that the spacecraft potential in reality may be a few volts less negative, in the vicinity of  $-13 \text{ V}$ , which would be in better agreement with the Langmuir probe measurements presented in Section 2.4. Furthermore, it is

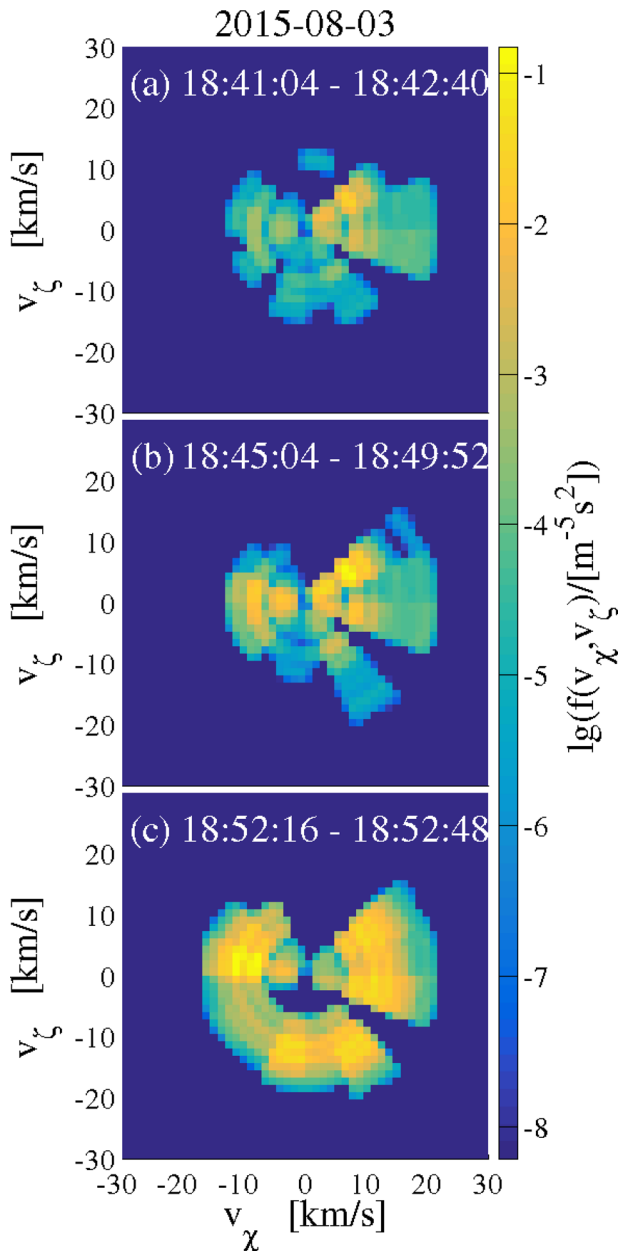


**Figure 5.** Two-dimensional water ion distribution functions. (a) Average of the six distributions recorded between 18:41:04 and 18:42:40 on 2015 August 3, that is, before the spacecraft entered the cavity. (b) Average of 18 distributions recorded inside the cavity between 18:45 and 18:50. (c) Average of two distributions recorded soon after the spacecraft left the cavity, between 18:52:16 and 18:52:48 on 2015 August 3.

seen in Fig. 2(d) that the energy of the ions increases during a few short periods, most noticeably at 18:51 when the spacecraft exited the diamagnetic cavity. This change in observed energy likely corresponds to a change in spacecraft potential, which is not precisely known.

The three distributions shown in Fig. 5 are all computed under the assumption of a  $-16.3$  V spacecraft potential, although the actual potential may have varied between the distributions and could be a few volts less negative. Fig. 5 shows the ion distributions before the spacecraft entered the cavity (top panel), while it was inside it (middle panel) and after it left the cavity (bottom panel).

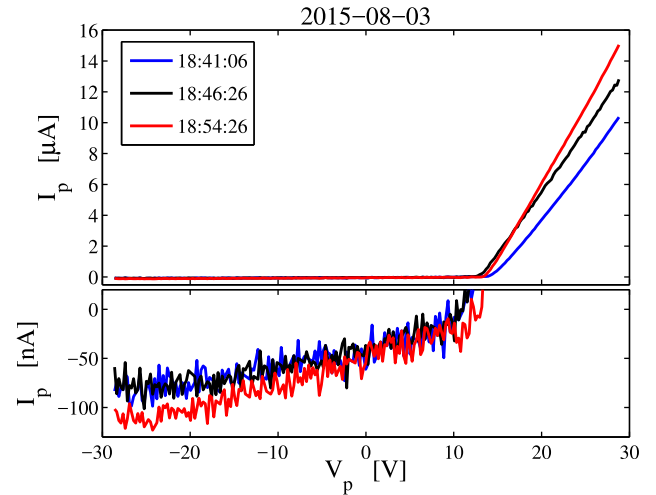


**Figure 6.** Langmuir probe current–voltage characteristics recorded by RPC-LAP probe 1 before the spacecraft entered the diamagnetic cavity (18:41, blue curve), while the spacecraft was in the cavity (18:46, black curve) and after the spacecraft had left the cavity (18:54, red curve). The upper panel shows the complete characteristic. In the lower panel, a different vertical scale is used in order to visualize the ion current.

The distribution has been rotated azimuthally to put the highest energy ions on the positive  $v_\chi$  axis. All three distributions shown have been rotated by the same angle. The low distribution function values in the upper ( $v_\zeta > 0$ ) part of all three panels correspond to sectors 10–13 that are blocked partially by the spacecraft body. The zero-flux segment diagonally down to the right ( $v_\chi > 0$ ,  $v_\zeta < 0$ ) corresponds to sector 1, which has a particularly low sensitivity.

The shape of the distribution function is the same in the three cases. The distribution in Fig. 5(c), recorded after the spacecraft left the cavity, but while it still was in the boundary region, is somewhat broader in velocity space. While such a broadening may indicate a higher ion temperature, it is more likely a result of a decreased spacecraft potential as discussed above. The hole in the distribution in Fig. 5(c) for  $-6 \text{ km s}^{-1} \lesssim v_\zeta \lesssim 0$  indicates an asymmetry in the sheath surrounding the negatively charged spacecraft caused by an electric field present in the boundary region of the diamagnetic cavity.

To estimate the ion density from the RPC-ICA measurements, assumptions must be made for the regions of velocity space that are outside the field of view. Assuming that the distributions are isotropic, we arrive at densities in the range of  $10^7$ – $10^8 \text{ m}^{-3}$  for the distribution shown in Fig. 5. This is one to two orders of magnitude lower than the plasma density observed by RPC-MIP shown in Fig. 2(c). To maintain quasi-neutrality, the vast majority of all ions must be hidden in the low-energy range that we do not observe when RPC-ICA is in the high temporal resolution mode with its reduced energy range.

The ion distributions are similar in the diamagnetic cavity and outside it. The dominating component is a cold distribution that we cannot measure directly. Ions are formed by ionization of the neutrals that emerge from the nucleus, and they will be cold in the absence of a heating process.

#### 2.4 Probe measurements of electron and ion populations

The upper panel of Fig. 6 shows Langmuir probe current–voltage characteristics obtained by RPC-LAP probe 1, before, during and after the cavity passage. The curves are similar to the one taken on

2015 July 30 that was analysed by Eriksson et al. (2017): the general shape of the curve is the same, the knee at which the sharp increase in current starts is at approximately the same probe potential, and the slope of the curve in the electron collecting regime is approximately the same. Following Eriksson et al. (2017), we make the interpretation that there is one cold ( $k_B T_e \lesssim 0.1$  eV) and one warm ( $5$  eV  $\lesssim k_B T_e \lesssim 10$  eV) electron population, and the spacecraft potential at the position of the probe, determined from the knee in the characteristic, is in the range of  $-14$  V  $\lesssim V_{sc} \lesssim -12$  V. The cold distribution is responsible for the steep slope of the characteristic, and the warm distribution charges the spacecraft negatively. The determination of how the density is distributed between the two populations, and of what the exact values of their temperatures are, is fraught with uncertainty. In Section 3, we examine how different assumptions about the particle populations affect the ion acoustic waves.

The lower panel of Fig. 6 shows the ion current part of the probe characteristics. The slope of the black and blue curves, which were recorded inside the cavity, is about  $2 \times 10^{-9}$  AV $^{-1}$ . For H<sub>2</sub>O<sup>+</sup> ions at  $n = 10^9$  m $^{-3}$  and a probe radius of 2.5 cm, this is consistent with a cold,  $T_i = 0$ , ion population with a bulk velocity of 1.7 km s $^{-1}$  (Mott-Smith & Langmuir 1926). Vigren & Eriksson (2017) obtained similar drift speeds in a 1D model of the ambipolar electric field.

### 3 WAVE THEORY

Since both the ion and electron distributions are known only approximately, we compute dispersion relations for five different assumed distributions to see what the consequences are for the generation of waves in the diamagnetic cavity. The computational method is based on simple pole expansions of the distribution functions (Löfgren & Gunell 1997; Tjulin, Eriksson & André 2000; Gunell & Skiff 2001, 2002; Tjulin & André 2002). It was reviewed by Gunell et al. (2017) in the context of waves at comets, also including computer programs to perform the calculation. Here, we only describe the distribution functions used in this work.

For the purpose of wave theory, the plasma is assumed to be unmagnetized. This is reasonable because the magnetic field is at most 1 nT, which means that the electron cyclotron frequency is below 28 Hz, which in turn is below the range of the observed waves. The gyro radii for a 0.1 eV electron and a 0.01 eV H<sub>2</sub>O<sup>+</sup> ion are more than 1 km and 61 km, respectively. That is much greater than the wavelength of ion acoustic waves, which the following calculations show is of the order of 1–10 m.

In each of the five cases shown in Table 1, we include three populations: H<sub>2</sub>O<sup>+</sup> ions, cold electrons and warm elec-

trons. Each population is described by an approximate drifting Maxwellian

$$M(v) = \left[ 1 + \frac{(v - v_d)^2}{2v_t^2} + \dots + \frac{1}{m!} \left( \frac{(v - v_d)^2}{2v_t^2} \right)^m \right]^{-1}, \quad (1)$$

where  $M$  is the reciprocal of a Taylor expansion of  $\exp\left(-\frac{(v - v_d)^2}{2v_t^2}\right)$ ,

$v_d$  is the average drift velocity,  $v_t$  is the thermal speed and  $m$  is the number of terms included in the expansion. Here, we have used  $m = 5$  for each of the two electron populations, and  $m = 6$  for the ion population. We compute the dispersion relations in the ion rest frame,  $v_{di} = 0$ . Assuming quasi-neutrality, the ion density is  $n_i = n_{ec} + n_{ew}$ , where  $n_{ec}$  and  $n_{ew}$  are the densities of the cold and warm electron populations respectively. The other parameters are shown in Table 1. In a plasma composed of different populations,  $\alpha$ , these are weighted by their respective plasma frequency squared to form the dielectric function (e.g. Krall & Trivelpiece 1973)

$$\epsilon(k, \omega) = 1 + \sum_{\alpha} \frac{\omega_{p\alpha}^2}{k^2} \int \frac{kdf_{\alpha}(u)/du}{\omega - ku} du. \quad (2)$$

For the normal modes, we assume a real value for the wavenumber  $k$  and a complex angular frequency  $\omega$ , which satisfies

$$\epsilon(k, \omega) = 0. \quad (3)$$

Distribution 1 in Table 1 is our nominal case, where none of the populations are drifting. The cold and warm electrons have equal densities. The dispersion relation is shown by the black curves in Fig. 7. The upper panels show the dispersion relations, given by the real part of  $\omega$  as a function of  $k$ , and the lower panels the damping rates  $\gamma$ . The right-hand panels show a zoomed-in view of the long wavelength range of  $0 \leq k \leq 5$  m $^{-1}$ . Only the ion acoustic modes are shown. Having two electron temperatures, these distributions can also support electron acoustic waves. However, since those would only be observable in a much higher frequency range than what we can measure, we do not show their dispersion relations. The black curves show that there are ion acoustic waves in the frequency range of the observations, but they also show that the damping is significant. Ion acoustic waves are heavily damped unless  $T_e \gg T_i$ . Here, we have chosen  $k_B T_i = 0.02$  eV, and a cold electron component with temperature,  $k_B T_e = 0.1$  eV, that is only five times higher.

Differing ion and electron drift velocities can be caused by an ambipolar electric field, as modelled by Vigren & Eriksson (2017), or by acceleration by an electric field arising in connection with the bulges on the boundary that are discussed in Section 4. The relative drift velocities used below are chosen in order to illustrate what

**Table 1.** Parameters of the electron and H<sub>2</sub>O<sup>+</sup> distributions for which dispersion relations are calculated and shown in Fig. 7.  $T_i$ ,  $T_{ec}$  and  $T_{ew}$  are the temperatures of the ions, the cold electrons and the warm electrons, respectively; the densities of the cold and warm electrons are  $n_{ec}$  and  $n_{ew}$ , respectively; and the corresponding drift velocities are  $v_{dec}$  and  $v_{dew}$ . In the last column, D means that the ion acoustic mode is damped and G that it is growing.

#	Ions		Cold electrons		Warm electrons			$J$ (nA m $^{-2}$ )	
	$k_B T_i$ (eV)	$k_B T_{ec}$ (eV)	$v_{dec}$ (km s $^{-1}$ )	$n_{ec}$ (m $^{-3}$ )	$k_B T_{ew}$ (eV)	$v_{dew}$ (km s $^{-1}$ )	$n_{ew}$ (m $^{-3}$ )		
1	0.02	0.1	0	$5 \times 10^8$	10	0	$5 \times 10^8$	0	D
2	0.02	0.1	8.7	$5 \times 10^8$	10	0	$5 \times 10^8$	697	G
3	0.01	0.1	2.0	$5 \times 10^8$	10	0	$5 \times 10^8$	160	G
4	0.01	0.1	1.6	$2 \times 10^8$	10	0	$8 \times 10^8$	51	G
5	0.02	0.1	8.7	$5 \times 10^8$	10	-8.7	$5 \times 10^8$	0	G

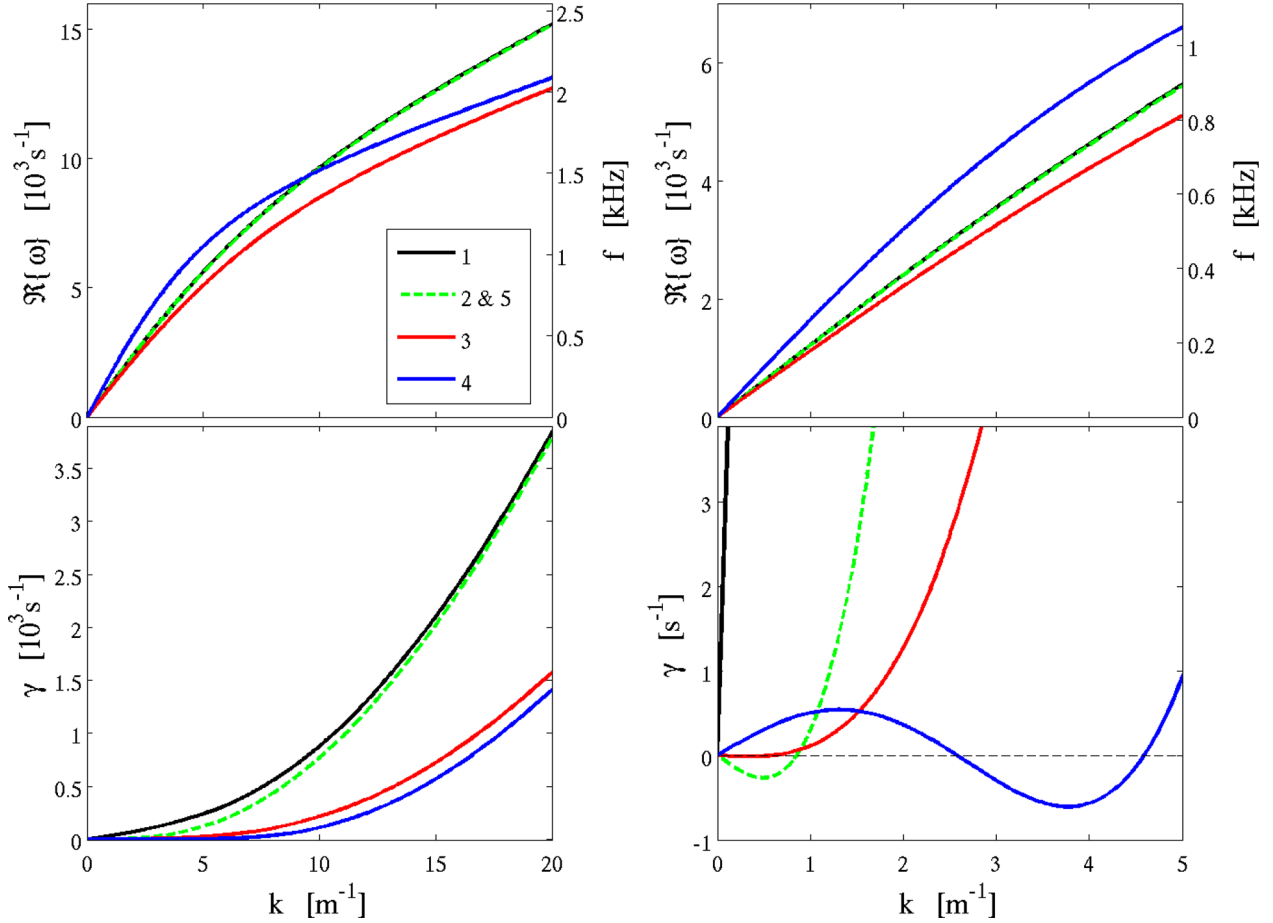


**Figure 7.** Dispersion relations (upper panels) and damping rates (lower panels) of ion acoustic waves computed for the distributions detailed in Table 1. The right-hand panels show a zoomed-in view of the long wavelength range of  $0 \leq k \leq 5 \text{ m}^{-1}$ . The results for distributions 2 and 5, being indistinguishably close, are shown by the same curve.

is required to drive the distribution unstable in the different cases. We have not tried to find the exact value of velocity that is on the border between stable and unstable distributions. By assigning a drift velocity of  $v_{\text{dec}} = 8.7 \text{ km s}^{-1}$  to the cold electrons we obtain distribution 2, shown by the dashed green curves in Fig. 7. The damping rate then becomes negative, which means that the wave is growing, for  $k \lesssim 1 \text{ m}^{-1}$ . The electrons are moving in the frame of the ions, and this corresponds to a current density of  $0.7 \mu\text{A m}^{-2}$  as shown in Table 1. Current-driven ion cyclotron waves have been observed in laboratory experiments (Sato et al. 1976; Michelsen et al. 1979), and the parameter regimes where these waves grow were mapped out theoretically by Stringer (1964). The magnetic field measurements show that  $B < 1 \text{ nT}$ . While the magnetic field depends on the current, wave growth depends on the current density. Thus, current-driven waves can be consistent with the magnetic field observations, if the spatial extent of the current channel is small enough. This is discussed further at the end of this section.

In distribution 3, the ion temperature has been lowered to  $k_B T_i = 0.01 \text{ eV}$ . That increases the electron to ion temperature ratio, and therefore the waves can be made unstable at a lower electron drift speed. The result is shown by the red curves in Fig. 7, where the red curve in the lower right-hand panel is below zero for  $0 < k < 0.6 \text{ m}^{-1}$ . Distribution 4 contains 20 per cent cold and 80 per cent warm electrons, instead of the equal numbers of warm and cold electrons in the other distributions. Distribution 4 is un-

stable at an even lower drift speed than distribution 3 and at a significantly lower current density. However, the maximum growth rate occurs at  $k \approx 3.8 \text{ m}^{-1}$ , as seen by the blue curve in the lower right-hand panel of Fig. 7. The upper right-hand panel shows that this corresponds to a frequency of approximately 860 Hz. Hence, the agreement with observations is worse for distribution 4 than for the other distributions, as all the spectra shown in Fig. 3 peak at significantly lower frequencies.

Finally, distribution 5 has all the same temperatures and densities as distribution 2; the cold electrons also have the same drift velocity. The difference is that the warm electrons have been given a drift velocity  $v_{\text{dew}} = -8.7 \text{ km s}^{-1}$ , counteracting the cold electron drift so that the net current is zero. The dispersion relation is so similar to that of distribution 2 that the curves cannot be distinguished on the scales of any of the panels in Fig. 7, and therefore both cases are shown by the dashed green curves. This example shows that it is the drift of the cold population that is important for dispersion relations and wave growth. This is a result of the large difference in thermal speeds between the two electron distributions, which renders a fixed drift speed more influential on the slope of the total distribution function when it is applied to the cold than to the warm electron population. It is not likely that such an unstable zero-current distribution would appear naturally at the comet, as that would require a mechanism that accelerates the two electron populations in opposite directions to exactly the same speed.

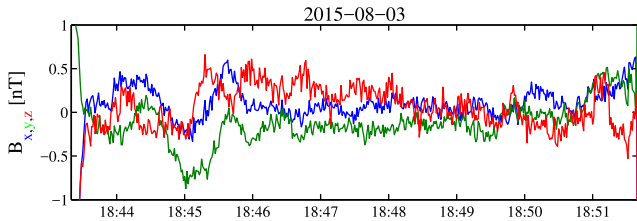


**Figure 8.** The three components of the magnetic flux density  $B$  seen by RPC-MAG for the cavity passage shown in Fig. 2.

The distribution functions of electrons and ions are not known precisely. From these examples of dispersion relations, we can draw the conclusion that the observed wave spectrum is consistent with ion acoustic waves in a plasma with two electron populations of different temperatures, where the cold population has a drift velocity with respect to the ions. The peak in the growth rate for the red and green curves in Fig. 7 is near  $k = 0.5 \text{ m}^{-1}$ , which corresponds to a wavelength of  $\lambda \approx 13 \text{ m}$ . For comparison, the Debye lengths of the cold and warm electron populations are  $0.1 \text{ m}$  and  $1 \text{ m}$ , respectively. The wave spectrum falls off with increasing frequency as shown in Fig. 3, and with the dispersion relations of Fig. 7,  $\lambda \approx 0.6 \text{ m}$  at  $1.5 \text{ kHz}$ .

The unstable distributions in Table 1 all carry a current, except distribution 5 which is a hypothetical example. The observations by Goetz et al. (2016a) confined the magnetic field to  $B < 1 \text{ nT}$ . The variation of the field inside the cavity is shown in more detail in Fig. 8 for the cavity observation between 18:43:20 and 18:51:43, which we use as an example in this paper. From Fig. 8, we conclude that  $1 \text{ nT}$  is a reasonable value of the maximum observed  $B$ . We can estimate the maximum size a current channel could have without generating higher magnetic fields than that. On the surface of a current-carrying slab of thickness  $d$ , the magnetic field is  $B = 0.5\mu_0 Jd$ , which means that for the  $J$  values 697, 160 and  $51 \text{ nA m}^{-2}$  in Table 1, the thicknesses  $d = 2.3, 9.9$  and  $31 \text{ km}$ , respectively yield a field of  $1 \text{ nT}$ .

#### 4 CONCLUSIONS AND DISCUSSION

We have observed wave spectra using the Langmuir probe instrument onboard the *Rosetta* spacecraft, when it was in the diamagnetic cavity of comet 67P/Churyumov–Gerasimenko. The wave spectrum peaks near  $200 \text{ Hz}$ . It falls off for higher frequencies, reaching the noise floor at approximately  $1.5 \text{ kHz}$ . The waves are seen only when the spacecraft is in the cavity or at its boundary. When the spacecraft is in the plasma outside the cavity, no waves are seen. We interpret these waves as ion acoustic waves in the water ion plasma of the comet. What generates these waves? We propose that they are driven by a current flowing through the plasma in the part of the diamagnetic cavity near the boundary, and that the spacecraft never went deep enough into the cavity to reach beyond this region. However, there are a few other possibilities that deserve a brief discussion.

The generation mechanism is unlikely to be an ion–ion instability, as we observe no sign of an ion beam in the data. There does remain a possibility that such a beam escapes detection, since the sensitivity of the ion instrument is low at low energies, and since, in the high temporal resolution mode used here, we have only two-dimensional ion measurements in one plane and an energy sweep that does not cover the lowest energies. If an ion beam exists, it would have to be generated in the same cold plasma that is dominating in the diamagnetic cavity, since a warmer beam, or one that has been

dispersed due to a distributed source region, would have a detectable ion tail.

An instability created by an anisotropic ion distribution cannot be ruled out completely, since the bulk of the ion distribution is at energies too low for us to observe directly. However, we find it unlikely that an anisotropy could be maintained in the unmagnetized plasma of the diamagnetic cavity. The anisotropy in Fig. 5(c), which we interpret as an indication of an anisotropic sheath around the spacecraft rather than an anisotropic ion distribution in the surrounding plasma, was measured outside the cavity and thus outside the region where ion acoustic waves are observed.

Another possibility is that the waves are indeed current driven, but only in the boundary layer itself, and that they propagate from the boundary into the cavity, but not away into the outside plasma. This hypothesis would require that the damping in the cavity to be significantly smaller than that on the outside of the boundary. It is possible that a heating mechanism could be active outside the boundary, leading to a warmer ion distribution there and hence to stronger damping. However, already distribution 1 in Table 1 at  $k_B T_i = 0.02 \text{ eV}$  shows significant damping, and in the absence of an electron drift one would expect considerable damping also in the cavity. Also, for this idea to hold, one would expect a decrease in wave power as the spacecraft moves away from the boundary farther into the cavity. There are a few isolated points of low power in the cavity in Fig. 4, but there is no systematic behaviour that could confirm the hypothesis. We deem it more likely that the source region of the wave extends to all the parts of the diamagnetic cavity that have been visited by *Rosetta*.

What could cause a spatially limited current channel consistent with these observations? The estimates in Section 3 put its thickness in a range from a few kilometres to a few tens of kilometres. The spacecraft was approximately  $220 \text{ km}$  from the nucleus when these observations were made. Thus, our estimates correspond to a thickness that is  $1\text{--}14$  per cent of the cavity radius. The values are approximate, but large-scale current closure through the centre of the cavity can be ruled out, as it would generate too strong a magnetic field. We can also dismiss the possibility that the current is confined to the outer regions of the cavity due to collisional resistivity in the interior. Using the neutral density of  $4 \times 10^{13} \text{ m}^{-3}$ , measured by the ROSINA-COPS instrument (Balsiger et al. 2007), and extrapolating inward using a Haser model, we estimate the resistivity to be insignificant everywhere except within  $10\text{--}20 \text{ km}$  from the nucleus.

Goetz et al. (2016a) performed a minimum variance analysis of the magnetic field at the cavity crossings and found the boundary normal direction to be consistent with elliptically shaped bulges on the boundary. Similarly, Henri et al. (2017) suggest that the parts of the boundary bend outward due to a Rayleigh–Taylor-like instability. If the boundary is pushed outward, forming a bulge, the magnetic field at the tip of the bulge would be stronger than at the sides of it. This means that the current in the boundary layer would have to be stronger at the peak of the protrusion, and some of that current could close through the bulging cavity. The spacecraft is not moving significantly in relation to the nucleus of the comet. It is therefore reasonable to assume that all the diamagnetic cavity observations presented here happened due to extrusions moving over an effectively stationary spacecraft. We propose that all our observations took place in bulges, and that currents are running through these protuberant parts, generating current-driven ion acoustic waves. The nature of the wave environment deeper inside the diamagnetic cavity will have to be determined by future space missions.



**ACKNOWLEDGEMENTS**

Work at the Royal Belgian Institute for Space Aeronomy was supported by the Belgian Science Policy Office through the Solar-Terrestrial Centre of Excellence, by PRODEX/ROSETTA/ROSINA PEA 4000107705 and by a FRIA grant of the F.R.S.-FNRS. Work at Umeå University was funded by Swedish National Space Board (SNSB) grant 201/15. The work on RPC-MAG was financially supported by the German Ministerium für Wirtschaft und Energie and the Deutsches Zentrum für Luft- und Raumfahrt under contract 50QP 1401. Work at LPC2E/CNRS was supported by ESEP, CNES and by ANR under the financial agreement ANR-15-CE31-0009-001.

The Rosetta data is available through ESA's Planetary Science Archive.

**REFERENCES**

- Balsiger H. et al., 2007, *Space Sci. Rev.*, 128, 745  
 Behar E., Nilsson H., Wieser G. S., Nemeth Z., Broiles T. W., Richter I., 2016a, *Geophys. Res. Lett.*, 43, 1411  
 Behar E., Lindkvist J., Nilsson H., Holmström M., Wieser G. S., Ramstad R., Götz C., 2016b, *A&A*, 596, A42  
 Cravens T. E., 1987, *Adv. Space Res.*, 7, 147  
 Eriksson A. I. et al., 2007, *Space Sci. Rev.*, 128, 729  
 Eriksson A. I. et al., 2017, *A&A*, in press  
 Glassmeier K.-H., 2017, *Phil. Trans. R. Soc. A*, 375, 2097  
 Glassmeier K.-H., Boehnhardt H., Koschny D., Kührt E., Richter I., 2007a, *Space Sci. Rev.*, 128, 1  
 Glassmeier K.-H. et al., 2007b, *Space Sci. Rev.*, 128, 649  
 Goetz C. et al., 2016a, *MNRAS*, 462, S459  
 Goetz C. et al., 2016b, *A&A*, 588, A24  
 Gunell H., Skiff F., 2001, *Phys. Plasmas*, 8, 3550  
 Gunell H., Skiff F., 2002, *Phys. Plasmas*, 9, 2585  
 Gunell H. et al., 2015, *Planet. Space Sci.*, 119, 13  
 Gunell H. et al., 2017, *A&A*, 600, A3  
 Gurnett D. A., Anderson R. R., Haeusler B., Haerendel G., Bauer O. H., 1985, *Geophys. Res. Lett.*, 12, 851  
 Haerendel G., 1987, *Geophys. Res. Lett.*, 14, 673  
 Haerendel G., Paschmann G., Baumjohann W., Carlson C. W., 1986, *Nature*, 320, 720  
 Henri P. et al., 2017, *MNRAS*, preprint ([arXiv:e-prints](#))  
 Karlsson T. et al., 2017, *Geophys. Res. Lett.*, 44, 1641  
 Koenders C., Glassmeier K.-H., Richter I., Ranocha H., Motschmann U., 2015, *Planet. Space Sci.*, 105, 101  
 Krall N. A., Trivelpiece A. W., 1973, *Principles of Plasma Physics*. McGraw-Hill, New York  
 Löfgren T., Gunell H., 1997, *Phys. Plasmas*, 4, 3469  
 Mandt K. E. et al., 2016, *MNRAS*, 462, S9  
 Michelsen P., Pecseli H. L., Juul Rasmussen J., Schrittwieser R., 1979, *Plasma Phys.*, 21, 61  
 Mott-Smith H. M., Langmuir I., 1926, *Phys. Rev.*, 28, 727  
 Nemeth Z. et al., 2016, *MNRAS*, 462, S415  
 Neubauer F. M. et al., 1986, *Nature*, 321, 352  
 Nilsson H. et al., 2007, *Space Sci. Rev.*, 128, 671  
 Nilsson H. et al., 2015a, *Science*, 347, aaa0571  
 Nilsson H. et al., 2015b, *A&A*, 583, A20  
 Nilsson H. et al., 2017, *MNRAS*, preprint ([arXiv:e-prints](#))  
 Odelstad E. et al., 2015, *Geophys. Res. Lett.*, 42, 10  
 Oya H., Morioka A., Miyake W., Smith E. J., Tsurutani B. T., 1986, *Nature*, 321, 307  
 Richter I. et al., 2015, *Ann. Geophys.*, 33, 1031  
 Richter I. et al., 2016, *Ann. Geophys.*, 34, 609  
 Rubin M., Gombosi T. I., Hansen K. C., Ip W.-H., Kartalev M. D., Koenders C., Tóth G., 2015, *Earth Moon Planets*, 116, 141  
 Sato N., Popa G., Märk E., Mravlag E., Schrittwieser R., 1976, *Phys. Fluids*, 19, 70  
 Scarf F. L., Ferdinand V., Coroniti V., Kennel C. F., Gurnett D. A., Ip W.-H., Smith E. J., 1986, *Science*, 232, 377  
 Simon Wedlund C. et al., 2016, *A&A*, 587, A154  
 Simon Wedlund C. et al., 2017, *A&A*, in press  
 Stenberg Wieser G. et al., 2017, *MNRAS*, preprint ([arXiv:e-prints](#))  
 Stringer T. E., 1964, *J. Nucl. Energy*, 6, 267  
 Tjulin A., André M., 2002, *Phys. Plasmas*, 9, 1775  
 Tjulin A., Eriksson A. I., André M., 2000, *J. Plasma Phys.*, 64, 287  
 Trotignon J. G. et al., 2007, *Space Sci. Rev.*, 128, 713  
 Vigren E., Eriksson A. I., 2017, *AJ*, 153, 150  
 Vigren E., Galand M., 2013, *ApJ*, 772, 33

This paper has been typeset from a  $\text{\TeX}/\text{\LaTeX}$  file prepared by the author.